Applied Materials Today 26 (2022) 101334

Contents lists available at ScienceDirect

Applied Materials Today

journal homepage: www.elsevier.com/locate/apmt

Selective laser melting of metal structures onto graphite substrates via a low melting point interlayer alloy

Arad Azizi[a], Xiaobo Chen[a], Feilin Gou[a], Fatemeh Hejripour[a], Jacob A. Goodman[a], In-Tae Bae[c], Srikanth Rangarajan[a], Charles L. Arvin[d], Bahgat G. Sammakia[a,b], Changhong Ke[a,b], Guangwen Zhou[a,b], Scott N. Schiffres[a,b,*]

[a] Department of Mechanical Engineering, Binghamton University, Binghamton, NY 13902, USA
[b] Materials Science and Engineering Program, Binghamton University, Binghamton, NY 13902, USA
[c] Small Scale Systems Integration and Packaging Center, Binghamton University, Binghamton, NY 13902, USA
[d] IBM Corporation, Hopewell Junction, NY 12533, USA

ARTICLE INFO

Article history:
Received 25 June 2021
Revised 23 November 2021
Accepted 19 December 2021

Keywords:
Dissimilar material bonding
Graphite-metal bonding
Selective laser melting (SLM)
Thermal transport in additive manufacturing
High heat flux electronics cooling

ABSTRACT

We demonstrate a process to selective laser melt a metal alloy directly onto graphite. The heat transfer applications of metal features printed onto annealed pyrolytic graphite are compelling, as pyrolytic graphite has the second highest in-plane thermal conductivity (>1500 W/m-K at room temperature) of any bulk material. While the bonding of metal alloys commonly used in selective laser melting (SLM) with graphite is relatively weak, the proper interlayer material drastically improves the wetting and bonding. The challenge is the alloys that typically bond to graphite require extended bonding times at elevated temperatures (minutes to hours), while the SLM process delivers only brief exposures to high temperatures (~100 μs). In this paper, we employ a Sn3Ag4Ti alloy that rapidly forms a nanometer-thin layer of TiC, as verified by transmission electron microscopy. The influence of graphite thermal properties on interfacial bond strength is shown by mechanical testing and simulations of selective laser melting.

1. Introduction

Graphite consists of strong graphene sheets with relatively weak interplanar Van der Waals bonding [1]. The thermal conductivity in the hexagonal basal plane is remarkable (>1500 W/m-K) [2], which makes it an attractive material for heat spreaders. These properties of graphite lead to cooling applications for wide-bandgap semiconductor devices [3], microprocessors [4–7], lasers [8], and electronic packages in aerospace [9–12]. The ability to additively manufacture onto pyrolytic graphite would be beneficial to thermal and non-thermal applications. Moreover, such a process could translate to polycrystalline graphite, which has excellent mechanical properties (Young's Modulus ~10 GPa; coefficient of thermal expansion ~5.9 × 10^{-6} K^{-1}) and a high isotropic thermal conductivity (up to 140 W/m-K) [1].

Joining of graphite to metals is challenging due to the non-wetting behavior (large contact angles) of most metals, high temperatures required for bonding, and thermal stresses at the interface. In the electronics industry, graphite is often metalized by electroless plating of NiB or NiP [13,14]. However, both coatings suffer from weak mechanical properties and often experience flaking. Direct bonding of metals to carbon-based materials, which include carbon composite and graphite, has been previously demonstrated with conventional interlayer brazing [15–19] and solid-state diffusion bonding [20]. In both processes joining occurs by an interfacial reaction, which results in modification of interfacial energies and consequently decreases the contact angle due to chemical bonding [21,22]. Wetting in these systems is limited by the diffusion of reactive elements and local reaction kinetics [23–25]. Therefore, the joint strength is strongly influenced by the concentration of reactive species, temperature, and pressure at the interface. Reactive metals, such as Ti, Ta, Zr and Nb (group IV and V), have been bonded to graphite by carbide formation at the interface [26]. Despite this literature on conventional bonding of graphite to metal, our literature search discovered no literature on bond-

SLM, selective laser melting; RMS, root mean square; SEM, scanning electron microscopy; SE, secondary electron; BSE, backscattered electrons; EDS, energy-dispersive X-ray spectroscopy; TEM, transmission electron microscopy; HRTEM, high-resolution transmission electron microscopy; C_P, specific heat capacity; *ED*, energy density; *P*, laser power; *S*, laser scanning speed; *H*, hatch distance; *L*, layer thickness; HAADF, high-angle annular dark field; STEM, scanning transmission electron microscopy; XRD, X-ray diffraction; CTE, coefficient of thermal expansion; E_a, activation energy; k_B, Boltzmann constant; *T*, absolute temperature; *V*, shear force; *A*, cross-sectional area; τ_{max}, maximum shear stress.

* Corresponding author:
E-mail address: sschiffr@binghamton.edu (S.N. Schiffres).

https://doi.org/10.1016/j.apmt.2021.101334
2352-9407/

ing graphite to metals via selective laser melting or laser welding from other researchers.

The conventional brazing literature show Sn-Ag-Ti alloys chemically bond to a wide variety of materials, including graphite, many metals, and ceramics, at temperatures between 200°C to 450°C and times on the order of minutes to hours [15,17]. The low melting point of the alloy results in less thermal stress at the joint upon cool down. In conventional brazing studies, the presence of 1-3 weight percent of Ti in the interlayer alloy enables the wetting of graphite by metals through the formation of a titanium carbide bonding layer [17,19]. Following the bonding of graphite to Sn-Ag-Ti, different metals can be bonded to Sn-Ag-Ti alloys by formation of solid solutions and intermetallics at the interface: Al by Al_2Ti, AlTi, and Al_3Ti [19,27,28], Cu by Cu_6Sn_5 and Cu_3Sn [29,30], steel by $FeSn_2$ [27]. The challenge with selective laser melting to bond a dissimilar substrate with Sn-Ag-Ti is that the conventional bonding time of the alloy is on the order of minutes to hours, while the selective laser melting process requires printing on the order of ~100 µs (approximate interaction time of the continuous wave laser with each voxel).

The multi-material selective laser melting (SLM) literature is relatively unexplored. However, the literature has investigated multi-metal printing between Cu, Al, Fe, and Ni alloys [31–33]. Some of these works printed metal onto different metal substrates [33], while others printed multi-metal composites through multi-powder feedstocks [31,32]. Prior work demonstrated the printing of metal-ceramic-metal composites via serrated interlocking, a purely physical bonding mechanism [34]. The authors report these physical bonds are susceptible to delamination due to the high thermal stresses during SLM. We did not find examples of chemical bonding in the limited metal to non-metal SLM printing literature, aside from our prior work printing metal onto silicon, ceramics, and glasses [35–37].

This paper elucidates the additive manufacturing and bonding of metal alloys onto graphite substrates via SLM. The primary challenges to accomplishing this include the short bonding time and thermal stresses. The conventional metal-graphite bonding times are very long, compared to the characteristic laser exposure period of a single voxel in selective laser melting (~100 µs) [38,39]. However, the localized high temperatures in SLM enables rapid interfacial reaction which can result in strong bonds. The concept of using selective laser melting to bond dissimilar materials [35–37,40] and the potential applications to heat transfer [41,42] have recently been introduced by the authors. In this process, the activation energy for interfacial reactions between dissimilar materials is provided by a localized laser heating source instead of a furnace. By employing Sn-Ag-Ti alloys, we demonstrate that Ti chemically bonds to carbon to form a few nanometer-thick TiC bonding layer. Combined with our prior work printing onto silicon [42], this process has important implications to electronics cooling because it enables the additive manufacturing of pyrolytic graphite thermal management devices directly onto silicon.

2. Material and methods

2.1. Materials and processing technique

All experiments were performed with Binghamton University's EOS M290 SLM system under a N_2 or Ar atmosphere with O_2 concentrations of less than 0.15%. Ag, Ti, and Sn powders of greater than 99% purity and respective average diameters of 8 µm, 10 µm, and 20 µm were mixed (Fig. 1b). Further discussion on the powder mixture and uniformity is included in the supplementary information (Fig. S1). Superfine isomolded graphite (isostatically pressed) (Graphtek LLC, Model #GM-10) and thermally-annealed pyrolytic graphite (Minteq International Inc., Model Pyroid® HT) were used as the SLM print substrate (Fig. 1a) [32,33].

The polycrystalline graphite samples were roughened by laser ablation using a laser power of 200 W and a scanning speed of 1000 mm/s (Fig. 1c). Optical profilometry (Veeco NT1100) confirmed this ablated ~60 µm of graphite and brought the surface to a roughness of ~30 µm root mean square (RMS). The roughened surface led to better adhesion by exposing a clean graphite surface and improving wetting behavior [21].

The wetting and bonding of metal onto graphite are enabled by the formation of a TiC interlayer, which is a dictated by the temperature, transport of Ti to the interface, and reactions of the species (in depth discussion in section 3.3.2). The SLM process parameters were varied to find the optimal laser processing parameters to provide the highest wetting and bonding strength between graphite and the alloy, while minimizing thermal stress. The laser power was varied from 30 to 200 W and laser scanning speeds varied from 800 to 6500 mm/s. The hatch spacing and layer thickness were held constant at 90 µm and 40 µm, respectively. The laser is rastered over the interlayer twice, the so called double exposure strategy, which adheres better due to greater time at elevated temperatures [35]. High throughput testing was carried out to evaluate the SLM process parameters.

2.2. Characterization of the substrates

The polycrystalline and pyrolytic graphite substrates were characterized by Raman spectroscopy, X-ray diffraction, and flash diffusivity in order to evaluate crystallographic and thermal properties. The details and results of these characterizations are provided in the supplementary information (Fig. S2, S3).

2.3. Characterization of the interlayer alloy

The ADMET eXpert 4000 Horizontal MicroTest System was used to measure the mechanical properties of three rectangular selective laser melted Sn3Ag4Ti alloy test specimens. The interlayer alloy thermal conductivity was previously studied with frequency domain thermoreflectance [35].

2.4. Microanalysis of the interface

Different modes of scanning electron microscopy (SEM) that include secondary electron (SE), backscattered electrons (BSE) and energy-dispersive X-ray spectroscopy (EDS) were used to examine the interface of the samples. For SEM studies, the graphite-alloy interfaces for both pyrolytic and polycrystalline samples were epoxied and fine wet polished with silicon carbide abrasive disks from 120 to 1200 grit; and then with 3, 1, and 0.25 µm diamond slurries, followed by a final 0.02 µm colloidal silica suspension. Transmission electron microscopy (TEM) characterization was performed using an FEI Talos F200X operating at 200 kV equipped with a four-quadrant energy dispersive X-ray spectroscopy (EDS) detector for elemental mapping. High-resolution TEM (HRTEM) and electron diffraction analyses were performed with a JEOL JEM 2100F microscope operating at 200 keV. Specimens for TEM were prepared using a focused ion beam system (FEI Helios Nanolab 600 Dual Beam).

2.5. Mechanical analysis of the interface

To characterize the small 3-D printed joints, shear tests were performed by the same method as our previous study of printing this alloy onto silicon [35]. Pins with average diameter of 0.35 mm were tested in shear using a bond tester (Nordson Dage 4000Plus Model with 5 kilograms-force load cell) with an offset height of

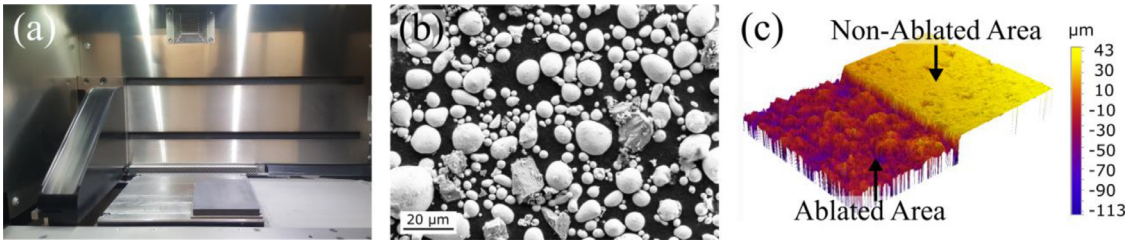

Fig. 1. (a) Polycrystalline graphite sample installed on a custom graphite build plate holder in the EOS M290. (b) Scanning electron microscope image of mixed Sn3Ag4Ti powder (EHT= 9kV, WD=8.6 mm, SE2 mode). (c) Optical profilometry of roughened polycrystalline graphite surface by laser ablation. The ablated surface area is 1.7 × 1.1 mm^2.

0.02 mm and shear speed of 0.1 mm/s. The number of samples measured on polycrystalline and pyrolytic graphite substrates for each process parameter were 12 and 19, respectively. The maximum shear stress values were calculated based on the shear formula for a circular cross section $\tau_{max} = \frac{4V}{3A}$, where V is shear force and A is the cross-sectional area of the cylinders deposited onto the graphite substrate [45].

2.6. Simulation of the SLM process

The domain consisted of a graphite substrate (5 × 2.5 × 0.5 mm) with a 40 μm powder layer on top of the substrate. A moving semi-elliptical heat source (q) with the laser power of 60 W and a laser scanning speed of 800 mm/s was used to melt the powder layer [46] and the powder absorptivity was assumed to be 36% [47]. The SLM simulations employed the default stainless steel 316L edge laser processing parameters, which were not modified for printing onto Sn3Ag4Ti. The solid-liquid phase transformation was implemented with an equivalent specific heat capacity (C_p) [48]. The energy loss due to the vaporization of the powder, convection, and radiation were considered in the heat transfer modeling [49]. The thermal conductivity was estimated to be 0.2 W/m-K for the powder [50] and 39.4 W/m-K for solidified region [35]. The remaining thermophysical properties of the powder were approximated based on pure Sn and Sn-Ag temperature-dependent data [51]. The thermal conductivities of the graphite substrates were based on our measurements, which are available in the supplementary information (Fig. S3). A finite element analysis was carried out using the COMSOL Multiphysics V5.5. The conservation of momentum and energy equations were solved in two domains that were linearly discretized using tetrahedral elements. A mesh independence study validated the chosen element sizes.

3. Results and discussion

3.1. Print process optimization

Sn3Ag4Ti powder was selective laser melted onto polycrystalline and pyrolytic graphite substrates in various geometries (Fig. 2). The laser energy density in selective laser melting is $ED=P/S \times H \times L$, where ED is the laser energy density (J/mm^3), P is the laser power (W), S is the laser scanning speed (mm/s), H is the hatch distance (mm), and L is the layer thickness (mm) [52]. A wide range of laser energy densities were tested for initial process development (5.77 J/mm^3 to 55.56 J/mm^3). In these experiments, the laser power, hatch distance and powder layer thickness were held constant while changing the laser scanning speed. A narrower range were tested for mechanical testing based on appearance from this screening test (7.24-9.46 J/mm^3). The entire multi-dimensional laser processing parameter space was not exhaustively studied due to its vastness. However, the trends versus volumetric energy density can be used to anticipate how the printing process would change for parameters not studied (*eg* scanning power, hatch spacing), though additional process parameter testing should be considered for future studies. The optimization criteria for these tests were based on visual observation of the deposited alloy onto the graphite substrate. The prints were evaluated for SLM induced defects such as lack of fusion, spattering, and oxidation. Furthermore, the selected process parameters with complete fusion were mechanically tested to evaluate the interfacial bond strength. The influence of each SLM process parameter on the print quality and bond strength should be investigated in future studies. Compared to polycrystalline graphite, pyrolytic graphite required larger laser energy densities, owing to its greater in-plane thermal conductivity. The optimum process parameters for polycrystalline graphite were at 7.24 J/mm^3 (laser power of 150 W, a laser scanning speed of 5750 mm/s). The optimal process parameters for pyrolytic graphite were at an energy density of 9.46 J/mm^3 (150 W, 4400 mm/s). Lower laser scanning speeds lead to a greater heating period and maximum temperature, improving the diffusion of reactants and assisting spreading. However, slower scanning results in more vaporization-induced defects (spattering and vaporization).

To demonstrate the fabrication of 3D metal structures, three layers of the Sn3Ag4Ti alloy with a thickness of 40 μm were deposited onto the graphite surface by SLM. The remaining Sn3Ag4Ti powders were extracted by a wet-separator to prevent cross-contamination. Afterwards, two layers of powder mixed with 50 wt% of stainless steel 316L were deposited with the same laser processing parameters to create an elemental gradient. Subsequent layers of stainless steel 316L were printed with EOS's default laser processing parameters for 316L support structure. Noteworthy, it is possible to automate this multistep manually deposition process by using alternative multi-material deposition systems [31,32]. The choice of material was due to its availability in our research facility. However, this would also work with higher thermal conductivity metals, such as AlSi10Mg (aluminum alloy), GRCop-42 (copper alloy), or pure copper, as desired for heat transfer applications. While printing pure copper in the ~1 μm laser wavelength is challenging, recent studies have shown the feasibility of printing copper with low laser powers (<500 W) [53,54]. These metals bond to Sn3Ag4Ti via intermetallic formation. Because printing stainless steel onto Sn3Ag4Ti leads to greater thermal stresses than Al and Cu alloys due to their greatly lower melting points, mechanical properties measured with stainless steel are anticipated to be conservative.

3.2. Thermal and mechanical properties of the interlayer alloy

Thermal conductivity of Sn3Ag4Ti alloy was previously studied with frequency domain thermoreflectance and found to be 39.4±6.7 W/m-K [35]. The thermal properties of materials fabricated by SLM are significantly affected by processing conditions and annealing [55–57]. Therefore, we suspect that with further process development, the thermal conductivity could potentially be

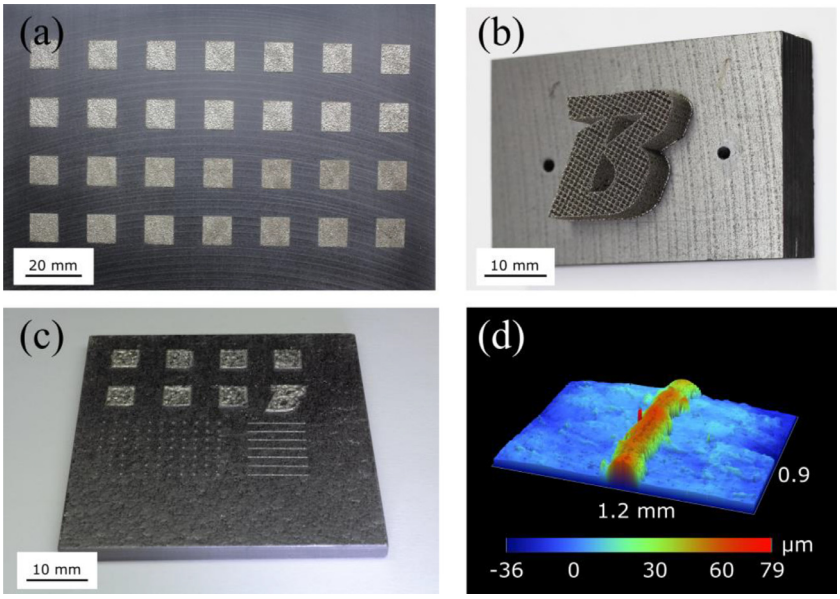

Fig. 2. (a) SLM process parameter study for Sn3Ag4Ti deposition onto polycrystalline graphite. (b) 316L stainless steel lattice structure printed by SLM onto polycrystalline graphite using Sn3Ag4Ti interlayer alloy. (c) Sn3Ag4Ti geometries deposited onto pyrolytic graphite. (d) A line of Sn3Ag4Ti deposited onto pyrolytic graphite surface viewed by optical profilometry.

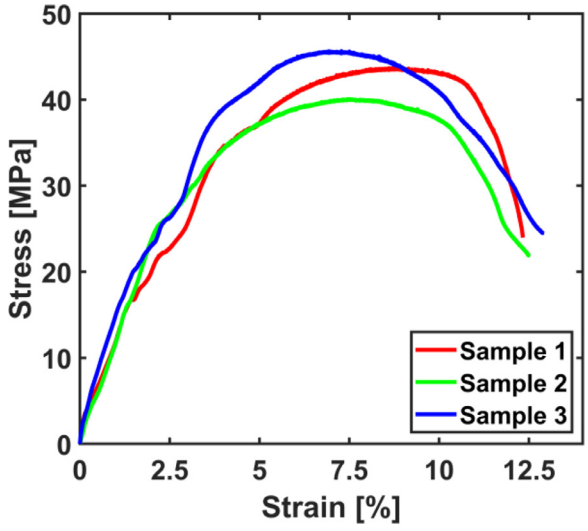

Fig. 3. The stress-strain curve for Sn3Ag4Ti samples fabricated by selective laser melting. The ultimate tensile strength is 43.1±2.8 MPa and Young's modulus is 3.2 ±1.4 GPa.

raised closer to the Sn value (73 W/m-K [58]), but that is outside the scope of this study.

The ultimate tensile strength (UTS) of 43.1±2.8 MPa and Young's modulus of 3.2 ±1.4 GPa were obtained for the laser-processed Sn3Ag4Ti alloy (Fig. 3). The UTS value was in good agreement with the tensile strengths of common lead-free solders that include Sn-3Ag-2Bi (54.7 MPa), Sn-3Ag-4Cu (48.3 MPa), and Sn-3Ag-2Sb (42.2 MPa) [58]. However, the selective laser melted samples were found to possess a much lower Young's modulus as compared with traditionally manufactured Sn3.5Ag (51.0 GPa) or pure Sn (44.5 GPa) specimens [59,60].

3.3. Characterization of the printed interface

3.3.1. Microanalysis of the interface

Polycrystalline graphite was chosen for high magnification study because it has a cleaner interface with less fracture and residues due to polishing. Pure Ti phases and Sn-Ti intermetallics are visible in Fig. 4a, where the darker color indicates Ti due to its relatively lower atomic mass than Sn and Ag. This is further confirmed by our EDS map in Fig. 4b. Quantitative EDS analysis provides a better understanding of the composition of elements at three locations of interest (Fig. 4c and table). A uniform mixing of Sn and Ag is observed in the matrix. Sn-Ti intermetallic phases can be clearly observed in Fig. 4 in both BSE and EDS images. The EDS shows a low concentration of titanium everywhere in the Sn-rich phase and clusters of titanium randomly distributed in the Sn alloy. To overcome the ~1μm electron interaction volume of SEM EDS, this interface was further characterized by transmission electron microscopy.

Fig. 5a illustrates a high-angle annular dark field (HAADF) scanning transmission electron microscopy (STEM) image that shows the typical morphology of the produced sample, which includes differently orientated grains (Sn-Ti phase) and the metal matrix (Ag-Sn phase). Fig. 5b shows the electron diffraction pattern obtained from the individual grain close to graphite, as marked with white dashed circle in Fig. 5a. The diffraction patterns in Fig. 5b indexes well with the structure of Sn_3Ti_5 phase, which is consistent with the XRD results in the literature [19,61]. Fig. 5c is the corresponding HRTEM image obtained from the grain marked with a dashed circle in Fig. 5a.

A zoomed-in HAADF STEM image of the interface at the location with a relatively higher concentration of Ti is provided in Fig. 6a. The distribution of elements can be seen in Fig. 6b-f. A clear Ti layer was observed at the interface in Fig. 6f which verifies the rapid diffusion and formation of a nanometers-thin TiC layer.

High magnification TEM at the interface of the Ti-rich layer and polycrystalline graphite (Fig. 7) was performed to study the distribution of elements and crystal structure of the wetting layer. The formation of TiC is expected, as it has been shown that bulk TiC composites can be formed by SLM [62,63]. This phase is also thermodynamically expected as formation energy per atom of TiC (-0.810 eV) is larger than Sn_3Ti_5 (-0.348 eV) [64,65,74].

The TEM image (Fig. 7a) reveals moiré fringes at the Ti-rich layer, which indicates crystallinity at the interface. Next, an EDS line scan across the interface (Fig. 7b) was performed to study

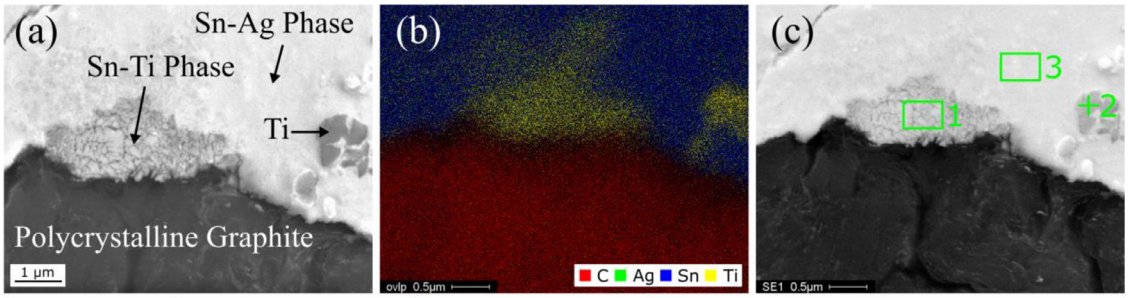

Element	C (K)		Ag (L)		Sn (L)		Ti (K)	
Measurement	Wt%	At%	Wt%	At%	Wt%	At%	Wt%	At%
1	06.55	31.06	00.24	00.13	59.26	28.44	33.95	40.38
2	10.67	40.76	00.40	00.17	45.67	17.65	43.25	41.42
3	03.83	27.80	00.68	00.55	94.18	69.26	01.31	02.39

Fig. 4. (a) Sn3Ag4Ti-polycrystalline graphite interface, Ti-Sn and Sn-Ag phases are observed [BSE mode, 12 kV, working distance (WD) 8.5 mm] (b) Sn3Ag4Ti-polycrystalline graphite interface showing concentration to Ti next to graphite (EDS mode, 12 kV, WD 8.5 mm) (c) Regions for quantitative EDS analysis marked in the image (SE mode, 12 kV, WD 8.5 mm) with the results in the table.

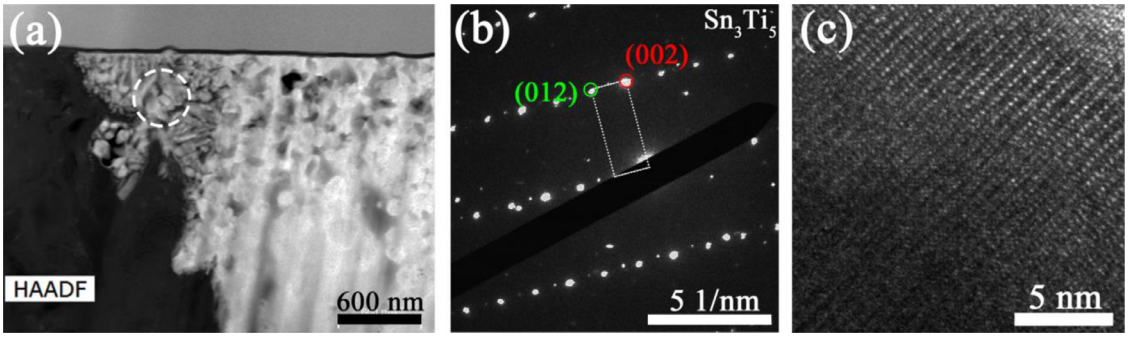

Fig. 5. TEM characterization of the Sn3Ag4Ti deposited onto polycrystalline graphite. (a) HAADF STEM micrograph showing the typical morphology. (b) Selected area electron diffraction pattern from the grain close to graphite. (c) HRTEM image obtained from the corresponding grain marked in (a).

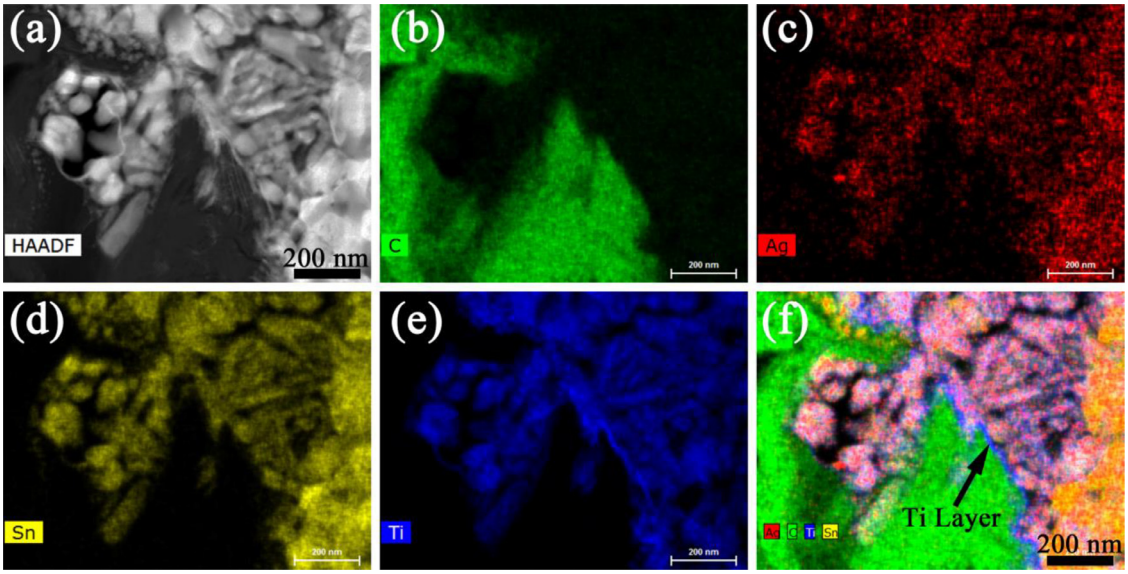

Fig. 6. TEM characterization of the Sn3Ag4Ti deposited onto polycrystalline graphite by HAADF STEM (a) and EDS map of C (b), Ag (c), Sn (d), Ti (e) and substitution overlay (f). Wetting of graphite with Ti is clearly observed in (f) with a ~10 nm Ti layer at the polycrystalline graphite-Sn3Ag4Ti interface.

compositional variations. High accumulation of Ti with the presence of carbon was observed at the interface, which provides further evidence of TiC phase formation. Next, a nano-beam electron diffraction (NBD) pattern (beam diameter of 8 nm) was obtained from a location on the Ti-rich layer indicated in Fig. 7a to verify the TiC phase formation (Fig. 7c). Finally, structure factor calculation for TiC showed great agreement to the interatomic spacings reported by the literature.[66]

3.3.2. Mechanical analysis of the interface

The reliability of the printed graphite-alloy bond is a function of the bonding strength of the joint. The median value for a group of

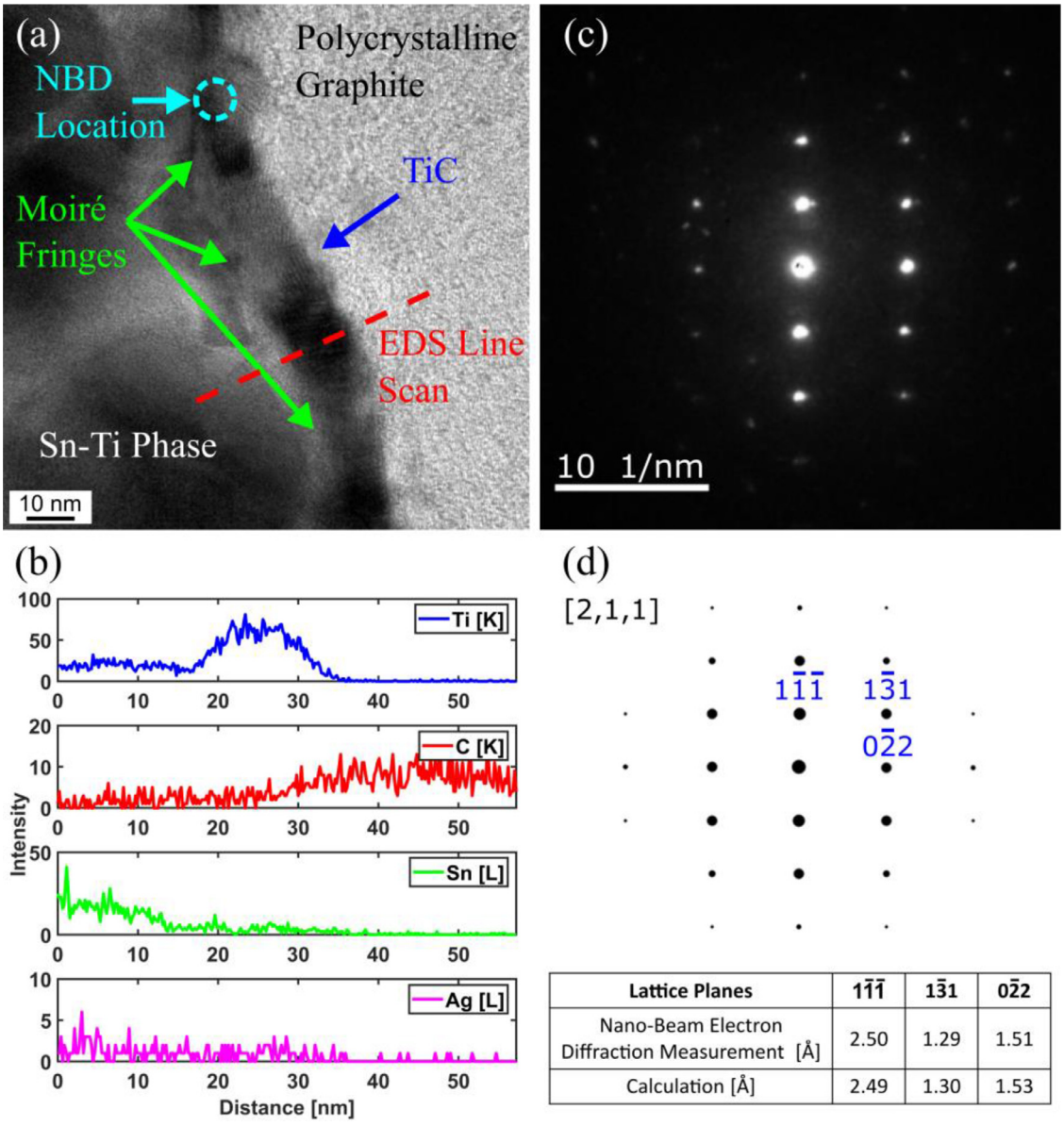

Lattice Planes	1$\bar{1}\bar{1}$	1$\bar{3}$1	0$\bar{2}\bar{2}$
Nano-Beam Electron Diffraction Measurement [Å]	2.50	1.29	1.51
Calculation [Å]	2.49	1.30	1.53

Fig. 7. (a) Presence of moiré fringes indicate crystallinity of the ~10 nm Ti-rich wetting layer observed via high magnification TEM imaging. (b) The EDS line scan shows a high concentration of Ti in a 10 nm layer, and the presence of C. (c) nano-beam electron diffraction pattern obtained from the wetting layer marked in (a) with a beam diameter of 8 nm. (d) the corresponding structure factor calculation of TiC demonstrates a good match between the obtained NBD pattern and literature [66].

samples that represent one process parameter was plotted (Fig. 8). A boxplot of interfacial strength versus scanning speed is shown in the SI (Fig. S4), which captures statistical uncertainty of the experiments. The maximum interfacial shear strength is 24 MPa for pyrolytic graphite and is 36 MPa for polycrystalline graphite. These values are compared to Ti-based brazing alloys bonded to graphite using non-localized heating *(i.e.*, without a laser) (Table 1). The laser scanning speeds were chosen based on earlier process parameter studies. It was observed that slower scanning speeds led to excessive vaporization and splattering defects, and faster speeds led to incomplete fusion and partial sintering.

The values obtained in the current study are in good agreement with literature values of interfacial strengths of Sn-Ag-Ti/graphite bonds obtained without laser processing [17,19]. The energy barrier for diffusion and crystallization must be overcome with thermal energy, as the reaction rate and Ti diffusivity are known to have an Arrhenius rate dependence, $exp(-E_a/k_BT)$, where E_a is the activation energy, k_B is the Boltzmann constant , and T is absolute temperature [69]. Due to the hot laser processing temperature, the energy barrier to atoms that diffuse and react can be overcome more rapidly than reactions just above the alloy melting point, which explains why this bonding occurs rapidly (~100 μs). The Gibbs free energy favors TiC over Sn-Ti intermetallics and pure Ti, but the formation of TiC is kinetically limited. Higher temperature induced by the SLM process accelerates the diffusion and reaction of Ti into TiC. Furthermore, rapid bond formation by SLM results in a decrease in TiC thickness at the Sn3Ag4Ti-graphite interface, which improves overall interfacial strength. Shrinking the thickness of the TiC layer changes the fracture mechanism at the interface from brittle to ductile failure, and consequently the interlayer can tolerate a larger stress [70–72].

Based on Fig. 8, pyrolytic graphite has a lower bond strength than polycrystalline graphite at all laser scanning speeds. Such variation stems from multiple factors: (1) High in-plane thermal conductivity of pyrolytic graphite results in rapid heat removal from the laser exposure location that results in shorter reaction

Table 1
Maximum interfacial shear strength of Ti-based interlayer alloys bonded to carbon materials.

Alloy nominal composition [wt%]	Processing method	Substrate	Interfacial shear strength [MPa]	Reference
Sn3Ag4Ti	Laser processed, microseconds	Polycrystalline graphite	18-36 *	Current study
Sn3Ag4Ti	Laser processed, microseconds	Thermally annealed pyrolytic graphite	16-24 *	Current study
Sn0.3Ag0.7Cu-(3%-5%)Ti	Brazing at 900-1050°C for 60-300 seconds	Polycrystalline graphite	19-24	[17]
Sn5Ag5Ti	Ultrasonic vibration-assisted brazing at 20 kHz and 500°C for 5 seconds and then gradual cool down in furnace	Polycrystalline graphite	~13	[19]
Ag35.2Cu1.75Ti	Brazing at 830-850°C for 300 seconds and then gradual cool down in furnace	Carbon fiber reinforced carbon composite	10-35 MPa	[67]
AgCu2Ti	Brazing at 830°C for 300 seconds at 9.7×10^{-5} Torr and then gradual cool down in furnace	Carbon fiber reinforced carbon composite	14-18 MPa	[67,68]

* The reported values are lower limit of interfacial shear strength.

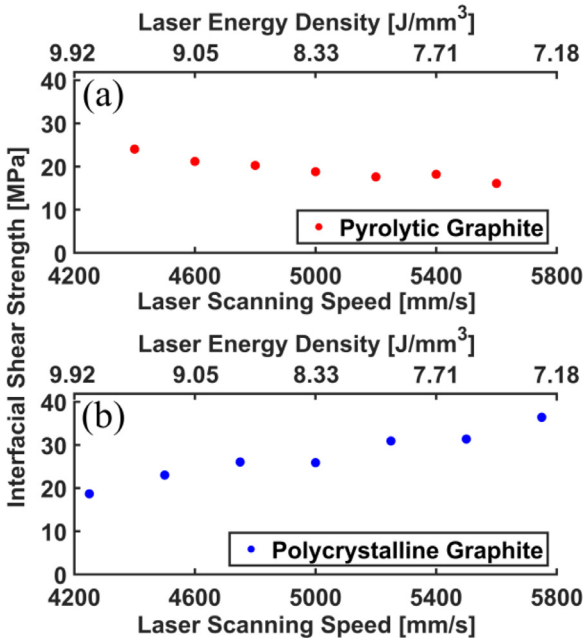

Fig. 8. (a) Shear tests of the bonding to pyrolytic graphite shows the maximum bonding strength at lower scanning speeds. (b) Shear tests of polycrystalline graphite demonstrate higher interfacial strength at faster laser scanning speeds than pyrolytic graphite. The laser power and hatch distance were kept at a constant value of 150 W and 0.09 mm, respectively. The data points reported for shear strength are median values.

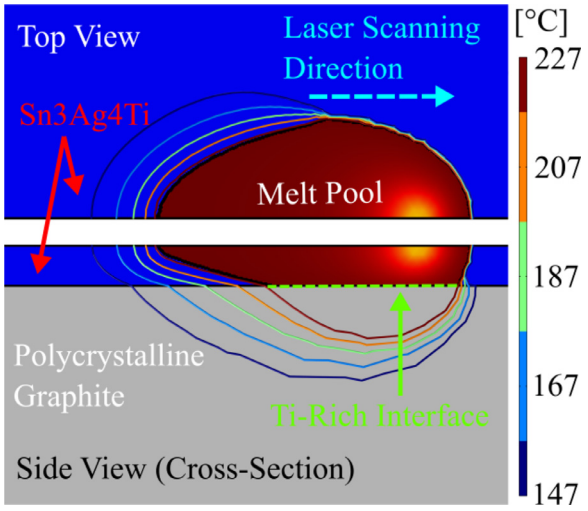

Fig. 9. Top view and side view (cross-section) of Sn3Ag4Ti layer deposition onto polycrystalline graphite by SLM. The location of the laser beam is visible in orange. An arrow is used to show the laser the scanning direction. Color coded temperature isotherms with legend are provided around the melt pool (red) and the graphite substrate (grey).

time and lower interfacial temperatures which limits reactive wetting; (2) The laser energy density influences the porosity of selective laser melted test balls, which directly affects interfacial shear strength values [55]; (3) The coefficient of thermal expansion (CTE) difference between the Sn3Ag4Ti alloy (approximated as Sn, 23×10^{-6} K^{-1} [58]) and pyrolytic graphite (in-plane, -0.4×10^{-6} K^{-1} [44]) is larger than that of polycrystalline graphite (5.9×10^{-6} K^{-1} [43]), which results in larger stresses at the interface during the solidification and cool down; (4) The polycrystalline graphite substrate has a 12% porosity, as compared to almost zero porosity reported for pyrolytic graphite [43,44]. The pores in polycrystalline graphite may act as an interlocking mechanism by penetration of the melt into the pores at the interface, which improves the bond strength. Among the mentioned factors for relatively lower bond strength in pyrolytic graphite, a high anisotropic thermal conductivity of pyrolytic graphite and a larger mismatch in CTE are expected to play the largest role. The opposite trends in shear strength versus laser scanning speed is due to the optimal volumetric energy density being greater for printing onto pyrolytic graphite than onto polycrystalline graphite, owing to the vastly different thermal conductivities of these substrates. The thermal conductivity influence on processing is further explored in the following simulation section.

3.3.3. Simulation of the SLM process

To demonstrate the effect of pyrolytic and polycrystalline graphite's thermal conductivity on the temperature of the bonding layer during the SLM process, two simulations of Sn3Ag4Ti alloy deposition were performed (Fig. 9). The temperature and heating/cooling rate for a point at the Sn3Ag4Ti-graphite interface in the central plane of the laser track is captured in Fig. 10. According to Fig. 10b, the maximum temperature for pyrolytic graphite (313 °C) is much smaller than that for polycrystalline graphite (632 °C), which limits the occurrence of interfacial reactions. Moreover, the temperature cannot simply be increased by increasing the laser power or slowing scanning speed, as higher laser energy densities will lead to vaporization defects. Furthermore, the period that the interlayer alloy is above the melting point is longer for polycrystalline graphite (270 µs) compared to pyrolytic graphite (170 µs). This leads to 60% increase in time for the intermetallic bond to form at the polycrystalline graphite interface. As a result, the pyrolytic graphite bond is weaker than polycrystalline graphite bond with the alloy. Because the simulation is for a single-laser line scan, the temperatures are lower than a print consisting of multi-

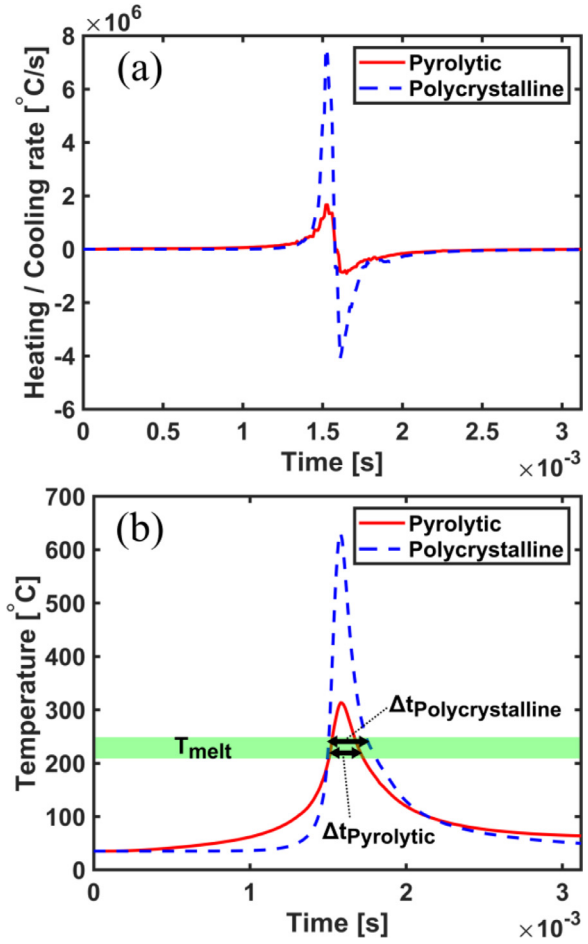

Fig. 10. Simulation results for (a) heating and cooling rates and (b) temperature at the Sn3Ag4Ti-graphite interface for a single-laser line scan. The maximum temperature at the pyrolytic graphite interface is 313 °C and at the polycrystalline graphite interface is 632 °C. The melting period at the interface for pyrolytic graphite is 170 µs and for the polycrystalline graphite interface is 270 µs.

ple scan lines [41]. Furthermore, our double laser exposure strategy (two consecutive laser rasters of the interlayer) was used to assist alloying and to increase the time of melting, which also affects the thermal history depending on the time between exposures.

3.4. Potential thermal applications

Printing metal onto pyrolytic and polycrystalline leads to many potential thermal applications. Pyrolytic graphite fins have higher conductivity than any other readily available bulk material. Fins made of pyrolytic graphite has a conductivity over 4X that of copper, which means pyrolytic graphite would have 2X lower thermal resistance than copper, assuming constant geometry, sufficiently long fins, and heat transfer coefficients that are held constant. This is owing to the thermal resistance of a long fin being proportional to the $k^{1/2}$, where k is thermal conductivity [73]. Because Sn3Ag4Ti has been shown to bond well to silicon [41], pyrolytic graphite could be laser welded vertically to silicon using a similar process as developed here. Fins or evaporative cooling wicks can be printed on top of pyrolytic graphite for hot spot heat spreading. The local heat spreading of pyrolytic graphite is excellent and can outperform copper, especially considering the lower thermal interface resistance posed by thinner pyrolytic graphite film. The detail of this analysis is explained in the supplementary information section 3 (heat transfer applications discussion).

5. Conclusion

We have demonstrated an additive manufacturing process that enables robust bonding of metals onto graphite. Common dissimilar material bonding takes several minutes to hours. However, in this process, the bonding timescale is in the order of ~100 µs. Our TEM inspection confirmed that the Ti element in the interlayer alloy diffused to the graphite interface and formed a 10 nm thin TiC layer during laser processing. The optimized process parameters for selective laser melting of Sn3Ag4Ti onto polycrystalline and pyrolytic graphite were shown to be different according to the shear test results. This variation comes mainly from extreme anisotropy in thermal conductivity and coefficient of thermal expansion of pyrolytic compared to polycrystalline graphite, which affects the temperature and thermal stresses at the interface. The influence of substrate thermal conductivity was later demonstrated by simulations that found the maximum temperature at the interface of pyrolytic graphite and polycrystalline graphite for identical process parameters. Both maximum temperature at the interface and the time of interfacial reaction for polycrystalline graphite are considerably greater compared to pyrolytic graphite.

By using this method, thermal management devices can integrate pyrolytic graphite with metals and silicon devices to improve thermal performance and reliability. Printing onto pyrolytic graphite may be desired for applications that demand high thermal conductivity and excellent heat spreading, as the in-plane thermal conductivity exceeds 1500 W/m-K, while applications that require excellent mechanical and thermal shock resistance with moderate thermal transport could benefit from polycrystalline graphite.

Author contributions

S.N.S. conceived the initial idea of this research. S.N.S, G.Z., C.K, B.G.S., and C.L.A. contributed to advising the work. A.A. designed and developed the alloy and processing technique, and performed sample fabrications, SEM characterizations, XRD, Raman Spectroscopy, shear tests, thermal, mechanical, and chemical analysis. X.C., G.Z. and I.B. performed FIB and analyzed the sample with TEM. F.G. and C.K. contributed to mechanical testing and analysis. F.H. performed COMSOL simulations for the flash diffusivity measurement and selective laser melting. J.G. performed flash diffusivity testing and analysis and helped with sample preparations. S.R. and B.G.S. contributed towards thermal applications and analysis. C.L.A. provided guidance regarding potential applications to electronics packaging. All authors contributed to the writing of this paper.

CRediT author statement

Arad Azizi: Conceptualization, Methodology, Validation, Formal analysis, Investigation, Writing - Original Draft, Visualization, Software. **Xiaobo Chen:** Formal analysis, Investigation, Validation, Visualization, Writing - Original Draft. **Feilin Gou:** Formal analysis, Investigation, Validation, Writing - Original Draft. **Fatemeh Hejripour:** Formal analysis, Investigation, Validation, Visualization, Software, Writing - Original Draft. **Jacob Goodman:** Investigation, Software, Writing - Original Draft. **In-Tae Bae:** Formal analysis, Investigation, Visualization, Writing - Original Draft. **Srikanth Rangarajan:** Conceptualization, Formal analysis, Writing - Original Draft. **Charles L. Arvin:** Conceptualization, Supervision, Writing - Original Draft. **Bahgat G. Sammakia:** Conceptualization, Methodology, Supervision, Funding acquisition, Resources, Writing - Original Draft. **Changhong Ke:** Conceptualization, Methodology, Supervision, Funding acquisition, Resources, Writing - Original Draft. **Scott N. Schiffres:** Project administration, Conceptualization, Methodol-

ogy, Supervision, Funding acquisition, Resources, Writing - Original Draft.

Data availability

The raw data required to reproduce these findings are available to download from [https://drive.google.com/drive/folders/1pdKPpnGfpgnRZOdINmtTha6l8IkRa8IV?usp=sharing]. The processed data required to reproduce these findings are available to download from [https://drive.google.com/drive/folders/1F4sQocraP23KGUGFhOxAEHCMCoM6moV4?usp=sharing].

Declaration of Competing Interest

Several of the authors have a prior patent application related to the work.

Acknowledgment

We gratefully acknowledge National Science Foundation (NSF) 1941181 (SNS, C.K., B.G.S) and 1846157 (S.N.S) awards. We thank Dr. Junghyun Cho for use of various sample preparation tools, Mr. Benson Chan and Dr. Stephen Cain at Binghamton University's Integrated Electronics Engineering Center for their support. We thank Scott Volk and Shawn Leonard for providing technical advice on the EOS M290. S.N.S also gratefully acknowledges SUNY Binghamton for providing support through his start-up funds and the Small Scale Systems Integration and Packaging (S3IP) Center of Excellence, funded by New York Empire State Development's Division of Science, Technology and Innovation. X.C. and G.Z acknowledge the support by the National Science Foundation (NSF) under the NSF Collaborative Research Award grant DMR 1905422. F.G. and C.K. acknowledge the support by the National Science Foundation (NSF) under award CMMI 2009134.

Supplementary materials

Supplementary material associated with this article can be found, in the online version, at doi:10.1016/j.apmt.2021.101334.

References

[1] M. Inagaki, F. Kang, Materials Science And Engineering Of Carbon: Fundamentals, Butterworth-Heinemann, 2014.
[2] G.A. Slack, Anisotropic thermal conductivity of pyrolytic graphite, Phys. Rev. 127 (1962) 694–701, doi:10.1103/PhysRev.127.694.
[3] E. Gurpinar, S. Chowdhury, B. Ozpineci, W. Fan, Graphite-embedded high-performance insulated metal substrate for wide-bandgap power modules, IEEE Trans. Power Electron. 36 (2021) 114–128, doi:10.1109/TPEL.2020.3001528.
[4] M.S. El-Genk, H.H. Saber, Composite spreader for cooling computer chip with non-uniform heat dissipation, IEEE Trans. Compon. Packag. Technol. 31 (2008) 165–172, doi:10.1109/TCAPT.2008.916847.
[5] Thermal Technical Working Group, Heterogeneous Integration Roadmap, Chapter 20: Thermal, IEEE Electronics Packaging, Society (EPS) (2019) https://eps.ieee.org/images/files/HIR_2019/HIR1_ch20_thermal.pdf.
[6] S. Snyder, J. Thompson, A. King, E. Walters, P. Tyler, M.R. Weatherspoon, Thermally enhanced 3 dimensional integrated circuit (TE3DIC) packaging, in: 2014 IEEE 64th Electronic Components and Technology Conference (ECTC), Orlando, FL, USA, IEEE, 2014, pp. 601–608, doi:10.1109/ECTC.2014.6897347.
[7] C. Bachmann, A. Bar-Cohen, Hotspot remediation with anisotropic thermal interface materials, in: 2008 11th Intersociety Conference on Thermal and Thermomechanical Phenomena in Electronic Systems, Orlando, FL, USA, IEEE, 2008, pp. 238–247, doi:10.1109/ITHERM.2008.4544276.
[8] J. Fang, H. Zhang, Y. Zou, L. Shi, W. Li, Y. Xu, L. Jin, Y. Li, L. Xu, X. Ma, Thermal management of a semiconductor laser array based on a graphite heat sink, Appl. Opt. 58 (2019) 7708, doi:10.1364/AO.58.007708.
[9] B.N. Bhat, Aerospace Materials and Applications, American Institute of Aeronautics and Astronautics, Inc., Reston ,VA, 2018, doi:10.2514/4.104893.
[10] T.A. Inc, Graphite Fiber Thermal Straps (GFTS®), (2019). https://www.techapps.com/graphite-fiber-thermal-straps (accessed December 27, 2019).
[11] A. Juhasz, High Conductivity Carbon-Carbon Heat Pipes for Light Weight Space Power System Radiators, 6th International Energy Conversion Engineering Conference (IECEC), American Institute of Aeronautics and Astronautics, 2008, doi:10.2514/6.2008-5784.
[12] S. Kugler, Aluminum encapsulated APG high conductivity thermal doubler, in: 49th AIAA/ASME/ASCE/AHS/ASC Structures, Structural Dynamics, and Materials Conference, 16th AIAA/ASME/AHS Adaptive Structures Conference, 10th AIAA Non-Deterministic Approaches Conference, 9th AIAA Gossamer Spacecraft Forum, 4th AIAA Multidisciplinary Design Optimization Specialists Conference, 2008, p. 1861.
[13] J. Breen, J. Carr, G. Fix, J. Judge, Nickel Boron Coatings, RAYTHEON COMPANY MATERIALS ENGINEERING LABORATORY, MASSACHUSETTS, 1977.
[14] F. Caturla, F. Molina, M. Molina-Sabio, F. Rodríguez-Reinoso, A. Esteban, Electroless Plating of Graphite with Copper and Nickel, J. Electrochem. Soc. 142 (1995) 4084–4090, doi:10.1149/1.2048468.
[15] R.W. Smith; S-Bond Technologies LL. Process of using an active solder alloy, US6047876A, 2000.
[16] J.Y. Liu, S. Chen, B.A. Chin, Brazing of vanadium and carbon-carbon composites to stainless steel for fusion reactor applications, J. Nucl. Mater. 212–215 (1994) 1590–1593, doi:10.1016/0022-3115(94)91095-2.
[17] W. Fu, S.P. Hu, X.G. Song, J.X. Li, J. Cao, J.C. Feng, G.D. Wang, Wettability and bonding of graphite by Sn0.3Ag0.7Cu-Ti alloys, Carbon 121 (2017) 536–543, doi:10.1016/j.carbon.2017.06.030.
[18] Z. Zhong, Z. Zhou, C. Ge, Brazing of doped graphite to Cu using stress relief interlayers, J. Mater. Process. Technol. 209 (2009) 2662–2670, doi:10.1016/j.jmatprotec.2008.06.021.
[19] W. Yu, S. Liu, X. Liu, M. Liu, W. Shi, Interface reaction in ultrasonic vibration-assisted brazing of aluminum to graphite using Sn–Ag–Ti solder foil, J. Mater. Process. Technol. 221 (2015) 285–290, doi:10.1016/j.jmatprotec.2015.02.028.
[20] H. Sueyoshi, T. Nishida, Solid State Bonding of Graphite to SUS304 Steel, Mater. Trans. JIM 41 (2000) 414–419, doi:10.2320/matertrans1989.41.414.
[21] N. Eustathopoulos, M.G. Nicolas, B. Drevet (Eds.), Wettability at High Temperatures, Pergamon, 1999.
[22] D.P. Sekulić, Advances in Brazing Science, Technology and Applications, 1st ed., Woodhead Publishing, 2013.
[23] E. Saiz, A.P. Tomsia, Atomic dynamics and Marangoni films during liquid-metal spreading, Nat. Mater. 3 (2004) 903–909, doi:10.1038/nmat1252.
[24] N. Eustathopoulos, Progress in understanding and modeling reactive wetting of metals on ceramics, Curr. Opin. Solid State Mater. Sci. 9 (2005) 152–160, doi:10.1016/j.cossms.2006.04.004.
[25] Y. Tang, G. Li, Thermodynamic study of Sn-Ag-Ti active filler metals, Phys. Procedia 25 (2012) 30–35, doi:10.1016/j.phpro.2012.03.045.
[26] M. Tashiro, A. Kasahara, NEC Microwave Tube Ltd. Method of bonding graphite to metal, US5904287 A (1999).
[27] Q. Lin, W. Zhong, F. Li, W. Yu, Reactive wetting of tin/steel and tin/aluminum at 350–450 °C, J. Alloy. Compd. 716 (2017) 73–80, doi:10.1016/j.jallcom.2017.05.036.
[28] W.-L. Wang, Y.-C. Tsai, Microstructural characterization and mechanical property of active soldering anodized 6061 Al alloy using Sn–3.5Ag–xTi active solders, Mater. Charact. 68 (2012) 42–48, doi:10.1016/j.matchar.2012.03.007.
[29] R. Zhang, Y. Tian, C. Hang, B. Liu, C. Wang, Formation mechanism and orientation of Cu3Sn grains in Cu–Sn intermetallic compound joints, Mater. Lett. 110 (2013) 137–140, doi:10.1016/j.matlet.2013.07.116.
[30] J. Feng, C. Hang, Y. Tian, B. Liu, C. Wang, Growth kinetics of Cu6Sn5 intermetallic compound in Cu-liquid Sn interfacial reaction enhanced by electric current, Sci. Rep. 8 (2018) 1775, doi:10.1038/s41598-018-20100-1.
[31] C. Wei, L. Li, X. Zhang, Y.-H. Chueh, 3D printing of multiple metallic materials via modified selective laser melting, CIRP Ann. 67 (2018) 245–248, doi:10.1016/j.cirp.2018.04.096.
[32] A.G. Demir, B. Previtali, Multi-material selective laser melting of Fe/Al-12Si components, Manuf. Lett. 11 (2017) 8–11, doi:10.1016/j.mfglet.2017.01.002.
[33] M. Colopi, A.G. Demir, L. Caprio, B. Previtali, Limits and solutions in processing pure Cu via selective laser melting using a high-power single-mode fiber laser, Int. J. Adv. Manuf. Technol. 104 (2019) 2473–2486, doi:10.1007/s00170-019-04015-3.
[34] J. Koopmann, J. Voigt, T. Niendorf, Additive manufacturing of a steel–ceramic multi-material by selective laser melting, Metall. Mater. Trans. B 50 (2019) 1042–1051, doi:10.1007/s11663-019-01523-1.
[35] A. Azizi, M.A. Daeumer, S.N. Schiffres, Additive laser metal deposition onto silicon, Add. Manuf. 25 (2019) 390–398, doi:10.1016/j.addma.2018.09.027.
[36] S.N. Schiffres, A. Azizi; Research Foundation of State University of New York. Additive manufacturing processes and additively manufactured products, US20200047288A1, 2020.
[37] S.N. Schiffres, A. Azizi; Research Foundation of State University of New York. Additive manufacturing processes and additively manufactured products, US11167375B2, 2021.
[38] P.A. Hooper, Melt pool temperature and cooling rates in laser powder bed fusion, Additive Manufacturing 22 (2018) 548–559, doi:10.1016/j.addma.2018.05.032.
[39] P.J. DePond, J.C. Fuller, S.A. Khairallah, J.R. Angus, G. Guss, M.J. Matthews, A.A. Martin, Laser-metal interaction dynamics during additive manufacturing resolved by detection of thermally-induced electron emission, Commun. Mater. 1 (2020) 92, doi:10.1038/s43246-020-00094-y.
[40] A. Azizi, S.N. Schiffres, Laser metal additive manufacturing on graphite, in: Proceedings of the 29th Annual International Solid Freeform Fabrication Symposium – An Additive Manufacturing Conference. Reviewed Paper, Austin, TX, USA, 2018, pp. 2315–2324.
[41] A. Azizi, M.A. Daeumer, J.C. Simmons, B.G. Sammakia, B.T. Murray, S.N. Schiffres, Additive laser metal deposition onto silicon for enhanced microelectronics cooling, in: 2019 IEEE 69th Electronic Components and Tech-

nology Conference (ECTC), Las Vegas, NV, USA, IEEE, 2019, pp. 1970–1976, doi:10.1109/ECTC.2019.00302.
[42] V. Radmard, Y. Hadad, A. Azizi, S. Rangarajan, C.H. Hoang, C. Arvin, K. Sikka, S.N. Schiffres, B. Sammakia, in: Direct Micro-Pin Jet Impingement Cooling for High Heat Flux Applications, IEEE, San Jose, CA, USA, 2020, pp. 1–9, doi:10.23919/SEMI-THERM50369.2020.9142864.
[43] Isomolded Graphite Plate, Ground, 0.125"H. http://www.graphitestore.com/isomolded-graphite-plate-ground-0-125h (accessed January 6, 2020).
[44] Pyrolytic Graphite Plate, High Conductivity SN, 0.125"H. http://www.graphitestore.com/pyrolytic-graphite-plate-high-conductivity-sn-0-125h (accessed January 6, 2020).
[45] J. Gere, S. Timoshenko, Mechanics of Materials. 4th SI (1999).
[46] S. Kelly, S.S. Babu, S. David, T. Zacharia, A thermal and microstructure model for laser deposition of Ti-6Al-4V, in: TMS (The Minerals, Metals & Materials Society), Charoltte (2004) 45–52.
[47] C.D. Boley, S.C. Mitchell, A.M. Rubenchik, S.S.Q. Wu, Metal powder absorptivity: modeling and experiment, Appl. Opt. 55 (2016) 6496, doi:10.1364/AO.55.006496.
[48] E. Mirkoohi, D.E. Sievers, H. Garmestani, K. Chiang, S.Y. Liang, Three-dimensional semi-elliptical modeling of melt pool geometry considering hatch spacing and time spacing in metal additive manufacturing, J. Manuf. Process. 45 (2019) 532–543, doi:10.1016/j.jmapro.2019.07.028.
[49] R. Choo, J. Szekely, Vaporization kinetics and surface temperature in a mutually coupled spot gas tungsten arc weld and weld pool, Weld. J.(USA) 71 (1992) 77.
[50] L.C. Wei, L.E. Ehrlich, M.J. Powell-Palm, C. Montgomery, J. Beuth, J.A. Malen, Thermal conductivity of metal powders for powder bed additive manufacturing, Add. Manuf. 21 (2018) 201–208, doi:10.1016/j.addma.2018.02.002.
[51] T. Gancarz, Z. Moser, W. Gąsior, J. Pstruś, H. Henein, A comparison of surface tension, viscosity, and density of Sn and Sn–Ag alloys using different measurement techniques, Int. J. Thermophys. 32 (2011) 1210–1233, doi:10.1007/s10765-011-1011-1.
[52] F. Froes, R. Boyer (Eds.), Additive Manufacturing for the Aerospace Industry, Elsevier, 2019, doi:10.1016/C2017-0-00712-7.
[53] X. Lingqin, C. Guang, Z. Luyu, L. Pan, Explore the feasibility of fabricating pure copper parts with low-laser energy by selective laser melting, Mater. Res. Express. 7 (2020) 106509, doi:10.1088/2053-1591/abbd08.
[54] X. Yan, C. Chang, D. Dong, S. Gao, W. Ma, M. Liu, H. Liao, S. Yin, Microstructure and mechanical properties of pure copper manufactured by selective laser melting, Mater. Sci. Eng. 789 (2020) 139615, doi:10.1016/j.msea.2020.139615.
[55] J.C. Simmons, X. Chen, A. Azizi, M.A. Daeumer, P.Y. Zavalij, G. Zhou, S.N. Schiffres, Influence of processing and microstructure on the local and bulk thermal conductivity of selective laser melted 316L stainless steel, Add. Manuf. 32 (2020) 100996, doi:10.1016/j.addma.2019.100996.
[56] J. Simmons, M. Daeumer, A. Azizi, S.N. Schiffres, Local thermal conductivity mapping of selective laser melted 316L stainless steel, in: Proceedings of the 29th Annual International Solid Freeform Fabrication Symposium – An Additive Manufacturing Conference, Austin, TX, USA, 2018, pp. 1694–1707.
[57] P. Yang, L.A. Deibler, D.R. Bradley, D.K. Stefan, J.D. Carroll, Microstructure evolution and thermal properties of an additively manufactured, solution treatable AlSi10Mg part, J. Mater. Res. 33 (2018) 4040–4052, doi:10.1557/jmr.2018.405.
[58] T. Siewert, S. Liu, D.R. Smith, J.C. Madeni, Database for Solder Properties with Emphasis on New Lead-free Solders (Release 4.0) (2002).
[59] H. Tanaka, L.F. Qun, O. Munekata, T. Taguchi, T. Narita, Elastic properties of Sn-based Pb-free solder alloys determined by ultrasonic pulse echo method, Mater. Trans. 46 (2005) 1271–1273, doi:10.2320/matertrans.46.1271.
[60] Review and Analysis of Lead-Free Solder Material Properties: Sn-Ag-Cu Properties and Creep Data. https://www.metallurgy.nist.gov/solder/clech/Sn-Ag-Cu_Other.htm (accessed May 24, 2021).
[61] P. Pietrokowsky, P. Duwez, Crystal Structure of Ti5Si3,Ti5Ge3, and Ti5Sn3, JOM 3 (1951) 772–773, doi:10.1007/BF03397370.
[62] L. Lu, J.Y.H. Fuh, Z.D. Chen, C.C. Leong, Y.S. Wong, In situ formation of TiC composite using selective laser melting, Mater. Res. Bull. 35 (2000) 1555–1561, doi:10.1016/S0025-5408(00)00339-1.
[63] S. Dadbakhsh, R. Mertens, K. Vanmeensel, G. Ji, J.-P. Kruth, In situ transformations during SLM of an ultra-strong TiC reinforced Ti composite, Sci. Rep. 10 (2020) 10523, doi:10.1038/s41598-020-67434-3.
[64] Materials Data on Ti5Sn3 by Materials Project, (2015). https://doi.org/10.17188/1183578.
[65] Materials Data on TiC by Materials Project, (2016). https://doi.org/10.17188/1279030.
[66] Standard X-ray Diffraction Powder Patterns: Data for 58 substances (Vol. 25), US Department of Commerce, National Bureau of Standards, Washington, DC, 1981.
[67] T.-T. Ikeshoji, 13 - Brazing of carbon–carbon (C/C) composites to metals, in: D.P. Sekulić (Ed.), Advances in Brazing, Woodhead Publishing, 2013, pp. 394–420, doi:10.1533/9780857096500.2.394.
[68] H. Okamura, S. Kajiura, M. Akiba, Bonding between carbon fiber/carbon composite and copper alloy, Q. J. Jpn. Weld. Soc. 14 (1996) 39–46, doi:10.2207/qjjws.14.39.
[69] J.W. Mullin, Crystallization, 4th Edition, Butterworth-Heinemann, 2001.
[70] T. An, F. Qin, Relationship between the intermetallic compounds growth and the microcracking behavior of lead-free solder joints, J. Electron. Packag. 138 (2016) 011002, doi:10.1115/1.4032349.
[71] C. Yang, G. Xu, S.W.R. Lee, X. Zhang, Brittle fracture of intermetallic compounds in SAC solder joints under high speed ball pull/pin pull and Charpy impact tests, in: 2013 IEEE 63rd Electronic Components and Technology Conference, 2013, pp. 1294–1299, doi:10.1109/ECTC.2013.6575739.
[72] R. Tian, C. Hang, Y. Tian, J. Xu, Brittle fracture of Sn-37Pb solder joints induced by enhanced intermetallic compound growth under extreme temperature changes, J. Mater. Process. Technol. 268 (2019) 1–9, doi:10.1016/j.jmatprotec.2019.01.006.
[73] I. Lienhard J.H. (Ed.), A Heat Transfer Textbook Phlogiston Press, Cambridge, MA, 2020 http://ahtt.mit.edu.
[74] A. Jain, S.P. Ong, G. Hautier, W. Chen, W.D. Richards, S. Dacek, S. Cholia, D. Gunter, D. Skinner, G.K.A. Ceder, The Materials Project: A materials genome approach to accelerating materials innovationAPL, Materials 1 (1) (2013) 011002.doi:, doi:10.1063/1.4812323.